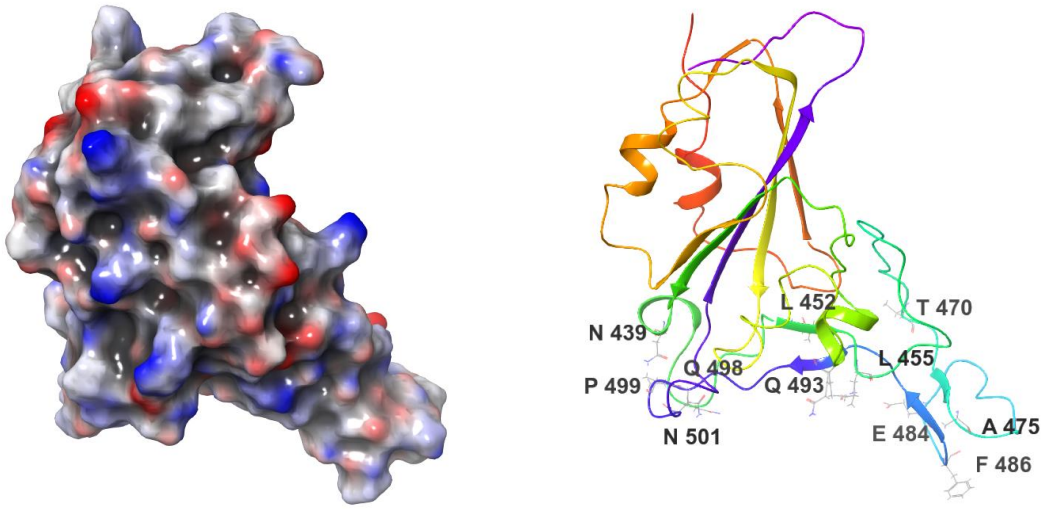

(**a**) (**b**)

Figure S1. Structure of the receptor-binding domain of wild-type SARS-CoV-2 (RBD-W) showing its (**a**) electrostatic potential map and (**b**) secondary structure, showing the critical residues surrounding the binding site of ACE2, which is the target of current drug discovery efforts.

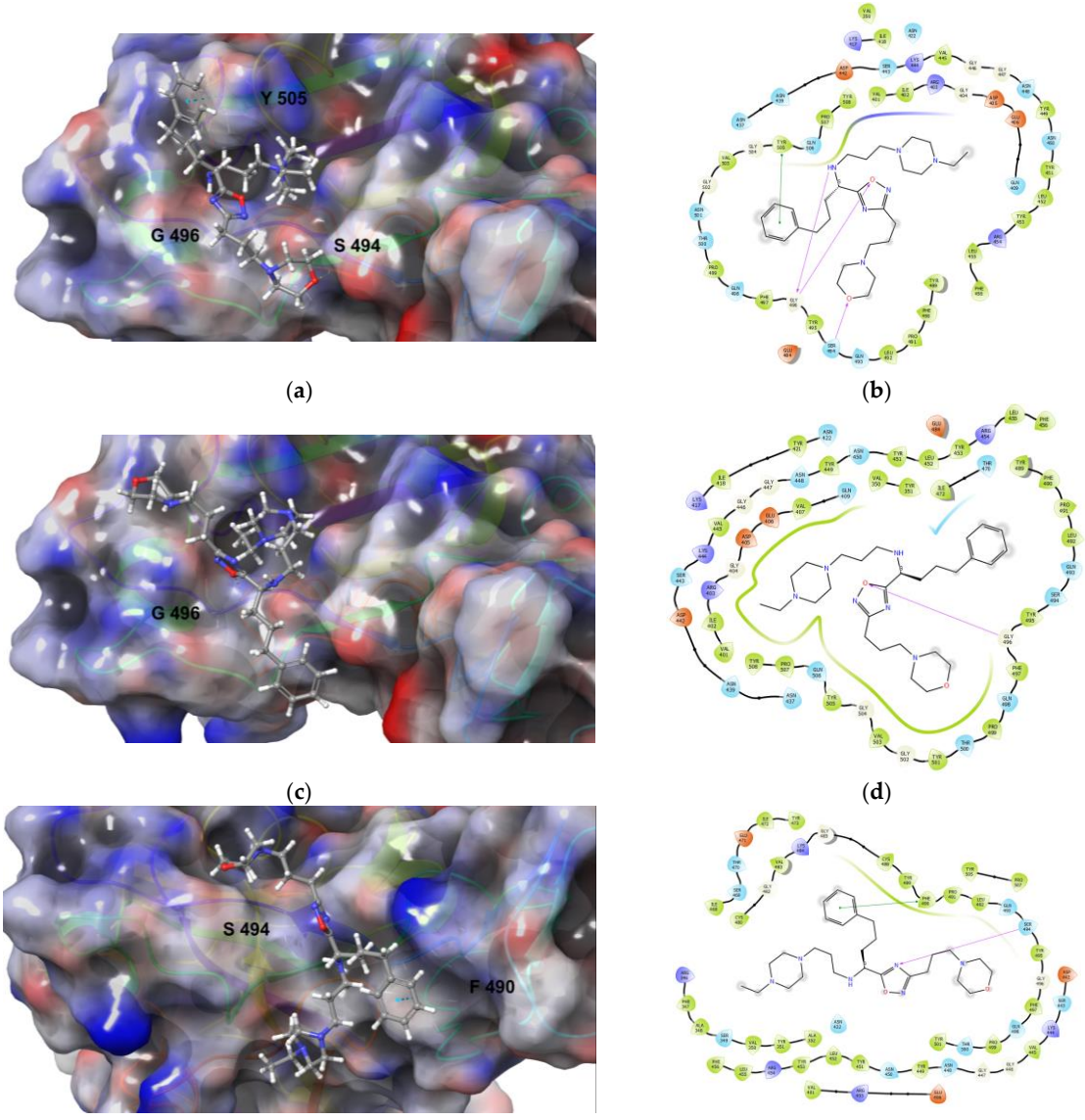

(**a**) (**b**)

(**c**) (**d**)

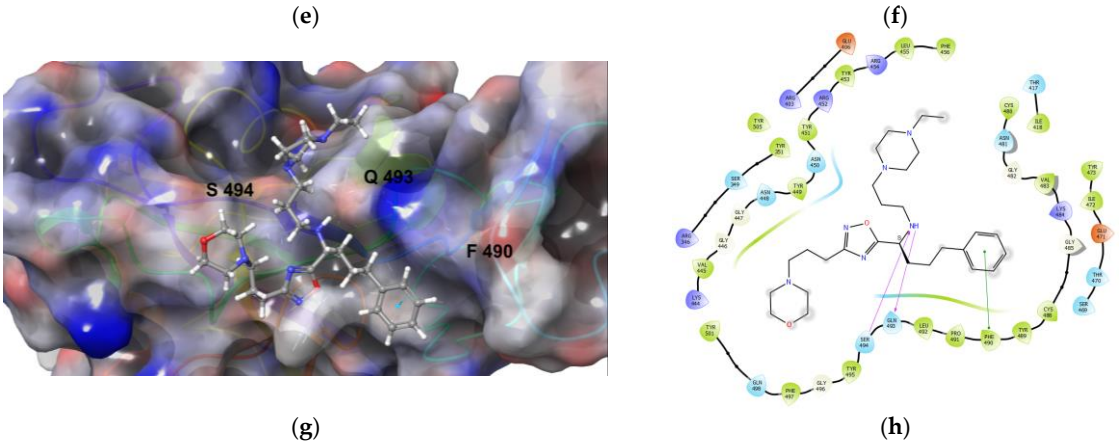

Figure S2. Structures of top-performing de novo generated drug-like molecule (Compound ID 526) docked in the RBD of SARS-CoV-2 and their corresponding ligand interaction diagrams: (**a**—**b**) wild type; (**c**—**d**) B.1.1.7 variant; (**e**—**f**) B.1.351 variant; and (**g-h**) P.1 variant.

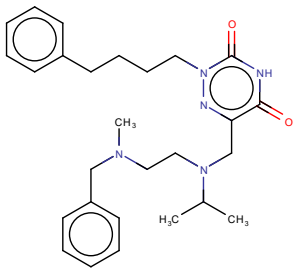

CID # 744

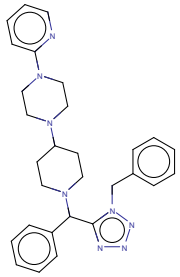

CID # 978

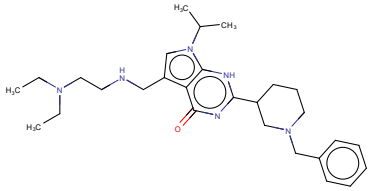

CID # 1650

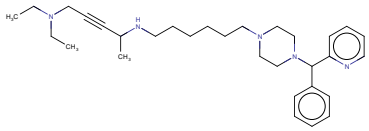

CID # 465

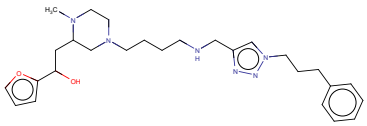

CID # 145

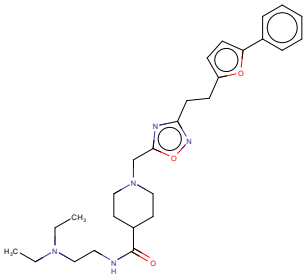

CID # 548

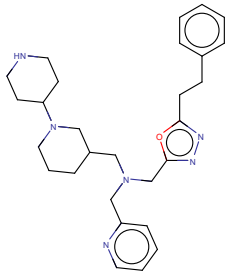

CID # 789

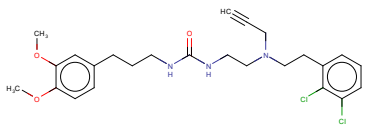

CID # 1530

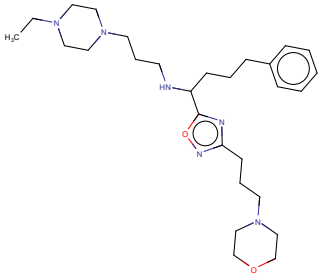

CID # 526

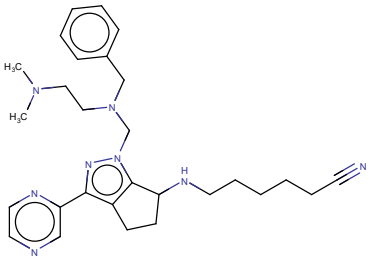

CID # 1635

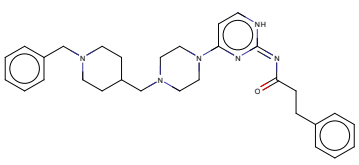

CID # 791

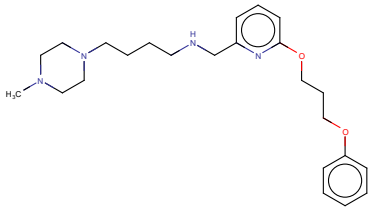

CID # 258

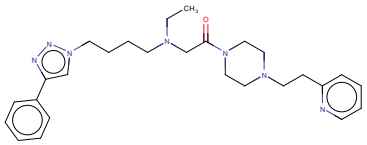

CID # 768

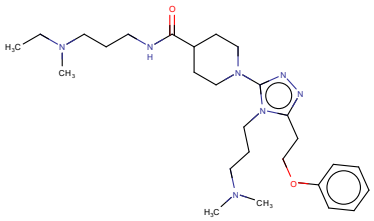

CID # 329

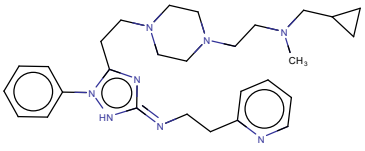

CID # 1152

Figure S3. Top-performing (1—15) drug-like molecules with respect to inhibiting the RBD of SARS-CoV-2 variants. These molecules were designed de novo using generative neural networks. The 2D structures were created using ChemAxon Marvin Suite.

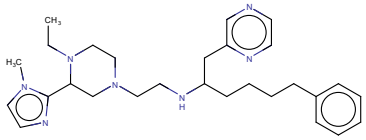

CID # 1575

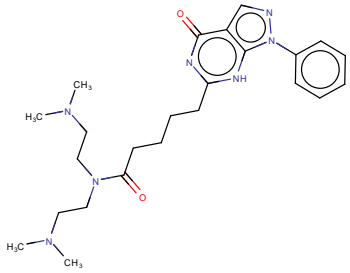

CID # 1127

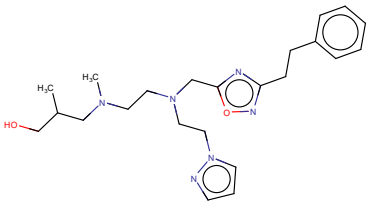

CID # 86

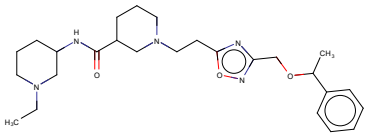

CID # 1700

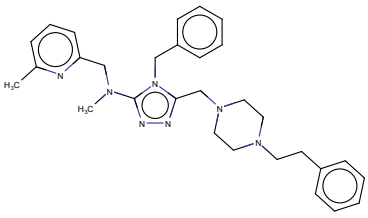

CID # 1056

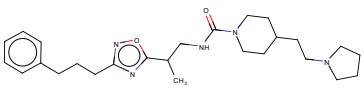

CID # 476

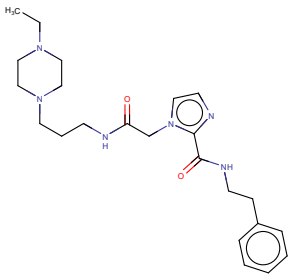

CID # 605

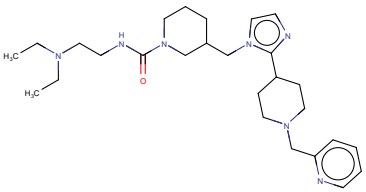

CID # 908

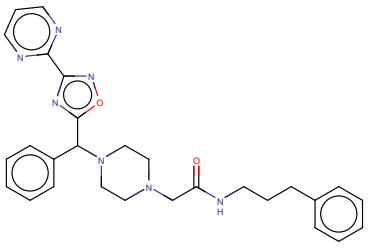

CID # 2267

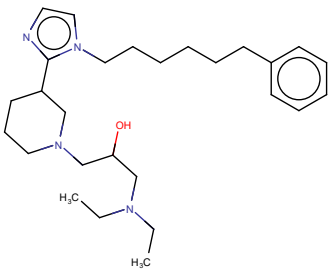

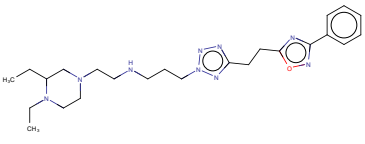

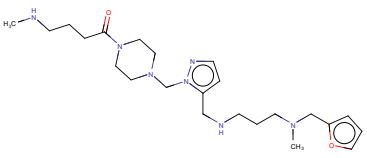

CID # 1615 CID # 1716 CID # 1133

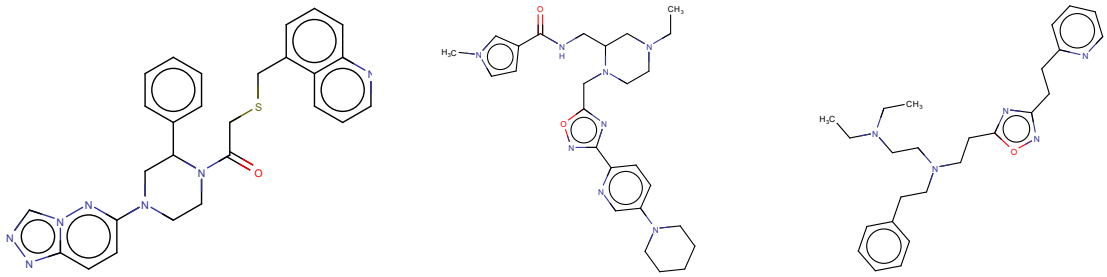

CID # 359 CID # 2131 CID # 425

Figure S4. Top-performing (16—30) drug-like molecules with respect to inhibiting the RBD of SARS-CoV-2 variants. These molecules were designed de novo using generative neural networks. The 2D structures were created using ChemAxon Marvin Suite.

Table S1. Comparison of the performance of top-performing de novo designed drugs in terms of their role as potential inhibitors of the RBD of SARS-CoV-2 variants.

Compound ID	Formula	Docking Score (%)					
		Wild	B.1.1.7	B.1.351	P.1	Mean	Std. Dev.
CID # 744	$C_{27}H_{37}N_5O_2$	91.61	93.72	93.27	93.48	93.02	0.96
CID # 978	$C_{29}H_{34}N_8$	92.63	93.18	93.29	91.97	92.77	0.61
CID # 1650	$C_{28}H_{42}N_6O$	92.58	92.45	93.25	92.76	92.76	0.35
CID # 465	$C_{31}H_{47}N_5$	92.76	91.96	92.95	92.31	92.50	0.45
CID # 145	$C_{27}H_{40}N_6O_2$	92.67	93.23	92.36	91.61	92.47	0.68
CID # 548	$C_{27}H_{37}N_5O_3$	92.57	92.36	92.41	92.43	92.44	0.09
CID # 789	$C_{28}H_{38}N_6O$	92.08	92.64	91.71	92.70	92.28	0.47
CID # 1530	$C_{25}H_{31}Cl_2N_3O_3$	91.53	92.77	92.83	91.99	92.28	0.63
CID # 526	$C_{28}H_{46}N_6O_2$	92.51	92.62	91.83	92.12	92.27	0.36
CID # 1635	$C_{28}H_{38}N_8$	91.06	92.72	92.52	92.60	92.23	0.78
CID # 791	$C_{30}H_{38}N_6O$	92.43	92.14	91.99	92.28	92.21	0.19
CID # 258	$C_{24}H_{36}N_4O_2$	90.99	93.28	91.89	92.65	92.20	0.99
CID # 768	$C_{27}H_{37}N_7O$	91.98	92.11	92.25	92.45	92.20	0.20
CID # 329	$C_{27}H_{45}N_7O_2$	92.62	91.95	91.72	92.40	92.17	0.41
CID # 1152	$C_{28}H_{40}N_8$	91.61	92.44	92.80	91.74	92.15	0.57
CID # 1575	$C_{28}H_{41}N_7$	92.28	91.41	92.30	92.12	92.03	0.42
CID # 1127	$C_{24}H_{35}N_7O_2$	91.91	92.21	91.21	92.61	91.99	0.59
CID # 86	$C_{23}H_{34}N_6O_2$	90.96	92.94	91.77	92.27	91.99	0.83
CID # 1700	$C_{26}H_{39}N_5O_3$	91.55	92.28	91.79	92.26	91.97	0.36
CID # 1056	$C_{30}H_{37}N_7$	91.57	92.55	91.79	91.88	91.95	0.42
CID # 476	$C_{26}H_{39}N_5O_2$	91.13	92.37	91.82	92.47	91.95	0.62
CID # 605	$C_{23}H_{34}N_6O_2$	91.48	92.18	92.11	91.92	91.92	0.31
CID # 908	$C_{27}H_{43}N_7O$	91.79	91.79	92.01	92.09	91.92	0.15
CID # 2267	$C_{28}H_{31}N_7O_2$	91.68	92.24	91.75	91.92	91.90	0.25
CID # 1615	$C_{27}H_{44}N_4O$	91.92	91.15	92.30	92.11	91.87	0.50
CID # 1716	$C_{24}H_{37}N_9O$	91.45	92.34	91.39	92.22	91.85	0.50
CID # 1133	$C_{23}H_{39}N_7O_2$	91.54	91.89	91.88	92.01	91.83	0.20
CID # 359	$C_{27}H_{25}N_7OS$	91.09	91.52	91.97	92.67	91.81	0.68
CID # 2131	$C_{26}H_{36}N_8O_2$	91.18	91.69	91.90	92.42	91.80	0.51
CID # 425	$C_{25}H_{35}N_5O$	91.51	91.95	91.67	92.05	91.80	0.25

Table S2. ADMET physicochemical properties of top-performing de novo designed drugs in terms of their role as potential inhibitors of the RBD of SARS-CoV-2 variants.

Compound ID	Physicochemical Properties

	Molar Mass (g mol^{-1})	Topological Polar Surface Area (A^3)	No. of Hydrogen Bond Donors	No. of Hydrogen Bond Acceptors	LogS (Solubility, mol/L)	LogP (Distribution Coefficient, mol/L)	$LogD_{7.4}$ (Distribution Coefficient, mol/L)
CID # 744	463.29	74.23	7	1	−2.487	3.298	3.238
CID # 978	494.29	66.21	8	0	−2.322	3.147	3.711
CID # 1650	478.34	69.19	7	2	−1.967	3.157	2.855
CID # 465	489.38	34.64	5	1	−2.113	3.866	3.758
CID # 145	480.32	82.59	8	2	−1.531	1.926	1.823
CID # 548	479.29	87.64	8	1	−3.134	3.438	3.329
CID # 789	474.31	70.32	7	1	−1.521	1.908	2.278
CID # 1530	491.17	62.83	6	2	−4.755	4.171	4.204
CID # 526	498.37	69.9	8	1	−1.925	2.457	2.377
CID # 1635	486.32	85.9	8	1	−1.504	1.910	2.133
CID # 791	498.31	67.83	7	1	−3.539	4.109	3.911
CID # 258	412.28	49.86	6	1	−2.604	2.905	2.464
CID # 768	475.31	70.39	8	0	−1.630	2.511	2.127
CID # 329	499.36	78.76	9	1	−2.122	2.126	2.023
CID # 1152	488.34	68.58	8	1	−2.004	2.608	2.032
CID # 1575	475.34	62.11	7	1	−1.348	2.108	2.564
CID # 1127	453.29	90.36	9	1	−1.642	0.964	1.337
CID # 86	426.27	83.45	8	1	−1.695	1.256	1.825
CID # 1700	469.31	83.73	8	1	−2.172	2.176	2.037
CID # 1056	495.31	53.32	7	0	−2.650	3.473	3.925
CID # 476	453.31	74.5	7	1	−3.892	3.882	3.481
CID # 605	426.27	82.5	8	2	−1.724	0.846	1.179
CID # 908	481.35	69.53	8	1	−1.153	1.635	1.346
CID # 2267	497.25	100.28	9	1	−2.255	2.715	3.389
CID # 1615	440.35	44.53	5	1	−3.249	4.094	3.443
CID # 1716	467.31	101.03	10	1	−1.826	2.186	2.511
CID # 1133	445.32	81.81	9	2	0.230	-0.283	0.044
CID # 359	495.18	79.52	8	0	−3.268	3.324	2.909
CID # 2131	492.3	95.56	10	1	−2.113	1.835	2.442
CID # 425	421.28	58.29	6	0	−2.281	3.210	2.803

Note: The empirical-based decision states of each property are represented with different colors (green: excellent; yellow: medium; red: poor).

Table S3. ADMET absorption, distribution, and excretion properties of top-performing de novo designed drugs in terms of their role as potential inhibitors of the RBD of SARS-CoV-2 variants.

Compound ID	Absorption			Distribution			Excretion
	$LogP_{app}$ (Caco-2 Perme-ability)	$LogP_{app}$ (MDCK Perme-ability)	Plasma Protein Binding (%)	Volume Distribution (L/kg)	Blood-Brain Barrier (Probability)	% Unbound in Plasma	Clearance (mL/min/kg)
CID # 744	−5.364	2.52E-05	83.998	2.364	0.807	12.193	10.892
CID # 978	−5.563	3.87E-05	88.453	1.777	0.748	8.316	6.954
CID # 1650	−5.461	7.94E-06	56.023	2.45	0.914	55.618	8.121
CID # 465	−4.949	9.78E-06	79.702	0.682	0.978	16.141	9.428
CID # 145	−5.589	8.14E-06	64.638	1.336	0.805	48.553	9.34
CID # 548	−4.997	1.52E-05	71.567	3.033	0.919	30.592	8.385
CID # 789	−5.516	1.17E-05	65.269	2.433	0.690	49.437	8.967
CID # 1530	−5.048	5.56E-05	96.360	2.35	0.992	0.980	8.254
CID # 526	−5.482	8.02E-06	53.464	1.069	0.630	47.909	7.05
CID # 1635	−5.496	7.42E-06	79.452	1.432	0.968	37.516	7.363
CID # 791	−5.456	1.75E-05	85.019	1.531	0.946	11.748	8.985
CID # 258	−5.092	9.75E-06	70.180	1.477	0.802	27.740	11.233

CID # 768	−5.683	3.42E-05	78.999	1.481	0.962	26.455	10.119
CID # 329	−5.370	6.92E-06	68.387	1.545	0.631	45.506	7.305
CID # 1152	−5.296	1.27E-05	68.135	1.054	0.858	35.218	9.607
CID # 1575	−5.532	1.33E-05	56.781	1.031	0.955	43.539	10.959
CID # 1127	−5.339	6.06E-06	79.225	2.081	0.944	36.630	5.044
CID # 86	−5.085	3.12E-05	82.581	1.471	0.903	23.950	9.665
CID # 1700	−5.002	1.07E-05	59.641	7.171	0.847	42.828	3.883
CID # 1056	−5.216	2.11E-05	90.604	1.623	0.806	4.262	8.517
CID # 476	−5.486	1.05E-05	93.881	2.133	0.800	5.681	5.962
CID # 605	−5.273	8.47E-06	51.239	1.869	0.977	52.166	8.937
CID # 908	−5.997	9.48E-06	47.007	1.457	0.802	52.220	7.811
CID # 2267	−5.081	3.49E-05	94.937	3.159	0.915	3.216	7.191
CID # 1615	−5.364	1.52E-05	65.867	5.515	0.652	28.494	11.927
CID # 1716	−5.039	1.37E-05	79.296	1.057	0.562	31.526	9.153
CID # 1133	−5.969	4.71E-06	64.854	1.701	0.888	51.219	4.219
CID # 359	−4.860	1.99E-05	96.531	1.924	0.585	1.893	6.446
CID # 2131	−5.219	7.74E-06	77.664	1.452	0.944	29.811	5.802
CID # 425	−4.858	1.98E-05	70.309	2.294	0.876	22.847	8.688

Note: The empirical-based decision states of each property are represented with different colors (green: excellent; yellow: medium; red: poor).

Table S4. ADMET metabolism and toxicity properties of top-performing de novo designed drugs in terms of their role as potential inhibitors of the RBD of SARS-CoV-2 variants.

Compound ID	Metabolism		Toxicity		
	Cytochrome 450 Inhibitor	Cytochrome 450 Substrate	hERG Blocker (Probability)	Human Hepatoxicity (Probability)	Ames Mutagenicity (Probability)
CID # 744	CYP2D6	CYP2C19, CYP3A4	0.826	0.482	0.007
CID # 978	CYP2D6, CYP3A4	CYP2C19, CYP3A4	0.739	0.961	0.019
CID # 1650		CYP3A4	0.824	0.776	0.301
CID # 465	CYP2D6	CYP2C19, CYP2D6, CYP3A4	0.430	0.945	0.017
CID # 145	CYP2D6	CYP2C19, CYP2D6, CYP3A4	0.557	0.454	0.051
CID # 548	CYP2D6	CYP2D6	0.872	0.545	0.075
CID # 789	CYP2D6	CYP2C19, CYP2D6, CYP3A4	0.845	0.784	0.013
CID # 1530	CYP2C19, CYP2D6, CYP3A4	CYP1A2, CYP2C19, CYP2C9, CYP2D6, CYP3A4	0.952	0.473	0.013
CID # 526		CYP2C19, CYP2D6, CYP3A4	0.399	0.565	0.037
CID # 1635		CYP2D6	0.312	0.798	0.016
CID # 791	CYP2D6	CYP2D6, CYP3A4	0.991	0.994	0.033
CID # 258	CYP2D6	CYP2C19, CYP2D6	0.906	0.236	0.018
CID # 768		CYP2D6	0.737	0.401	0.109
CID # 329		CYP2C19, CYP2D6, CYP3A4	0.212	0.070	0.419
CID # 1152		CYP2D6, CYP3A4	0.863	0.893	0.029
CID # 1575	CYP2D6, CYP3A4	CYP2C19, CYP2D6, CYP3A4	0.443	0.536	0.014
CID # 1127		CYP2C19, CYP2D6	0.230	0.302	0.009
CID # 86	CYP2D6	CYP2C19, CYP2D6, CYP3A4	0.517	0.839	0.074
CID # 1700		CYP2D6, CYP3A4	0.795	0.635	0.466
CID # 1056	CYP2D6	CYP2D6, CYP3A4	0.951	0.281	0.029
CID # 476	CYP2D6	CYP2D6	0.976	0.833	0.014
CID # 605			0.454	0.177	0.072
CID # 908		CYP2D6	0.460	0.242	0.016
CID # 2267	CYP2C19, CYP2C9, CYP2D6, CYP3A4	CYP2C9, CYP3A4	0.440	0.914	0.024
CID # 1615	CYP2D6	CYP2C19, CYP2D6, CYP3A4	0.813	0.265	0.123
CID # 1716	CYP2D6	CYP2C19, CYP3A4	0.814	0.913	0.358

CID # 1133		CYP2C19, CYP2D6	0.117	0.623	0.023
CID # 359	CYP2C19, CYP2C9, CYP3A4	CYP2C9, CYP3A4	0.628	0.980	0.056
CID # 2131		CYP2D6	0.666	0.937	0.036
CID # 425	CYP2D6	CYP2D6	0.898	0.695	0.030

Note: The empirical-based decision states of each property are represented with different colors (green: excellent; yellow: medium; red: poor).

Table S5. ADMET toxicity and drug-likeness properties of top-performing de novo designed drugs in terms of their role as potential inhibitors of the RBD of SARS-CoV-2 variants.

Compound ID	Toxicity		Drug-likeness			
	Carcino-genicity (Probability)	Respiratory Toxicity (Probability)	Drug-likeness Score	Synthetic Accessibility Score	MCE-18 Score	Natural Product-likeness Score
CID # 744	0.061	0.739	0.394	2.576	18.000	-1.145
CID # 978	0.053	0.984	0.39	2.876	96.600	-2.065
CID # 1650	0.031	0.965	0.406	3.312	74.227	-1.371
CID # 465	0.009	0.933	0.308	3.507	50.612	-1.149
CID # 145	0.097	0.979	0.343	3.485	63.810	-1.244
CID # 548	0.575	0.966	0.423	2.557	47.122	-1.915
CID # 789	0.153	0.953	0.48	3.156	79.698	-1.395
CID # 1530	0.066	0.946	0.321	2.558	14.000	-1.164
CID # 526	0.067	0.976	0.376	3.08	63.333	-1.328
CID # 1635	0.025	0.985	0.344	3.552	66.000	-1.24
CID # 791	0.092	0.994	0.515	2.75	58.047	-1.266
CID # 258	0.023	0.972	0.511	2.241	31.027	-1.399
CID # 768	0.481	0.991	0.375	2.52	44.000	-2.062
CID # 329	0.297	0.782	0.377	2.639	40.000	-1.846
CID # 1152	0.055	0.989	0.424	3.095	55.814	-1.557
CID # 1575	0.034	0.989	0.382	3.569	63.721	-0.763
CID # 1127	0.130	0.953	0.421	2.789	19.000	-1.443
CID # 86	0.814	0.788	0.423	3.206	32.000	-1.951
CID # 1700	0.477	0.961	0.572	3.533	72.767	-1.894
CID # 1056	0.084	0.983	0.331	2.553	54.878	-1.512
CID # 476	0.174	0.958	0.582	2.994	68.372	-1.508
CID # 605	0.051	0.845	0.524	2.331	35.657	-1.453
CID # 908	0.086	0.982	0.563	3.161	72.333	-1.997
CID # 2267	0.085	0.946	0.334	2.962	77.189	-1.65
CID # 1615	0.049	0.972	0.437	3.221	51.556	-1.097
CID # 1716	0.879	0.913	0.378	3.262	64.103	-2.099
CID # 1133	0.021	0.979	0.423	2.771	35.368	-1.916
CID # 359	0.606	0.406	0.352	3.184	94.030	-2.15
CID # 2131	0.948	0.938	0.512	3.331	89.700	-2.067
CID # 425	0.168	0.956	0.396	2.505	15.000	-1.681

Note: The empirical-based decision states of each property are represented with different colors (green: excellent; yellow: medium; red: poor).

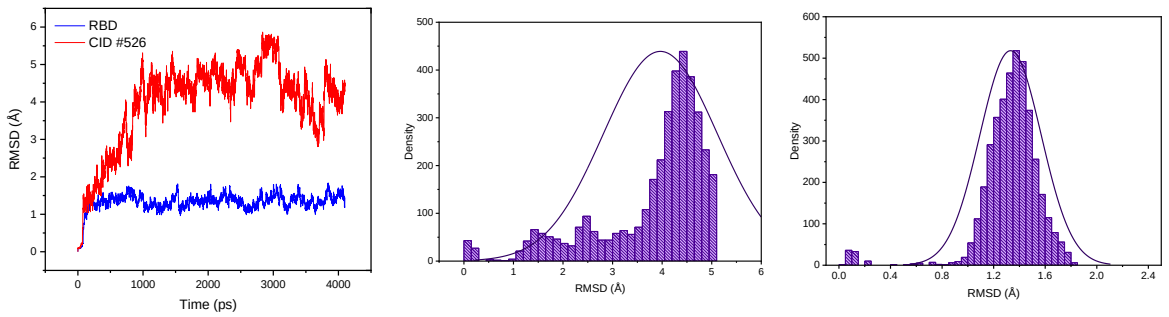

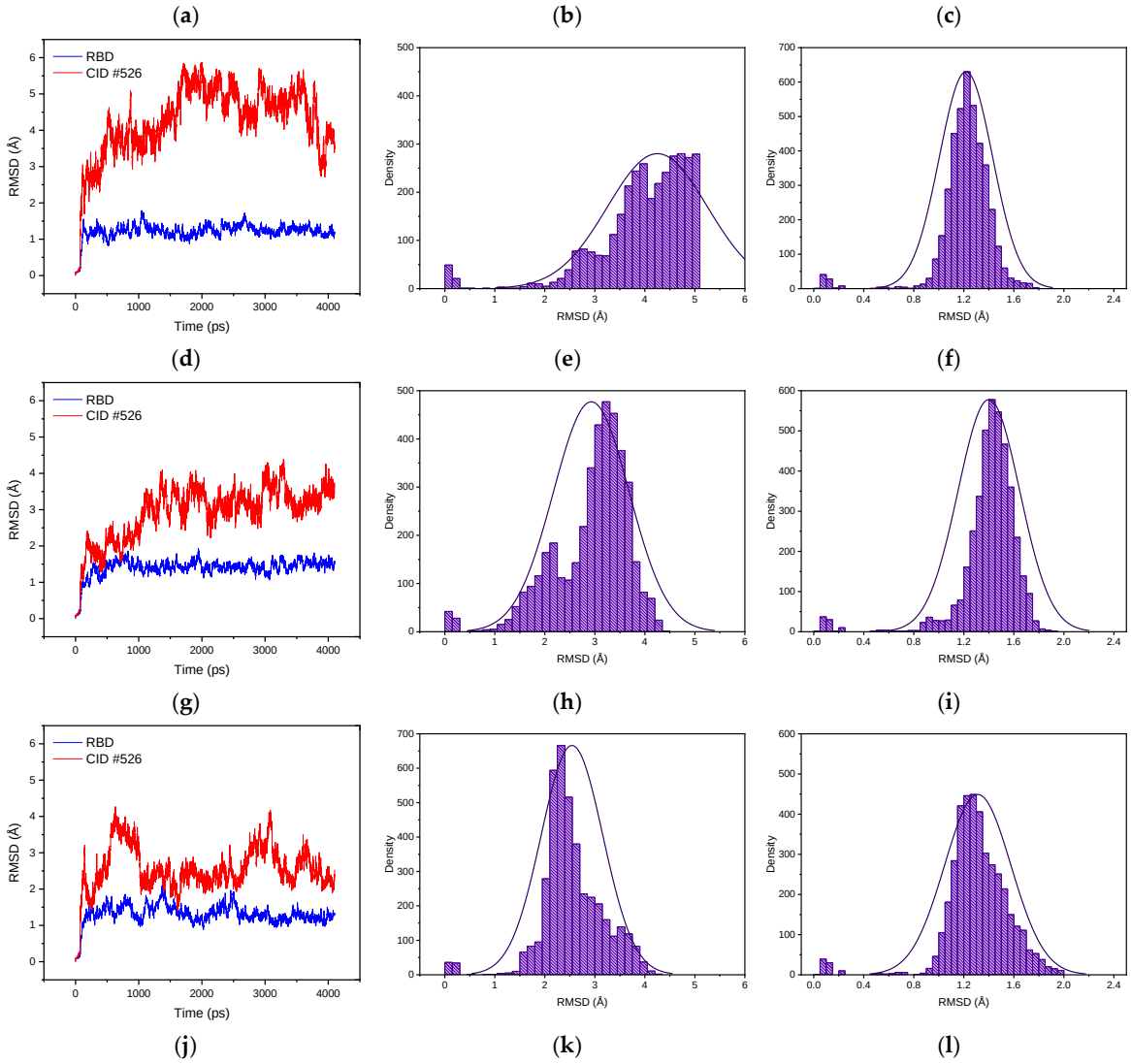

Figure S5. RMSD profiles of docked CID #526 designed using generative neural networks of the RBD, RMSD histogram of the ligand, and RMSD histogram of the receptor for (**a**—**c**) wild-type, (**d**—**f**) B.1.1.7 variant, (**g**—**i**) B.135 variant, and (**j**—**l**) P.1 variant of SARS-CoV-2.

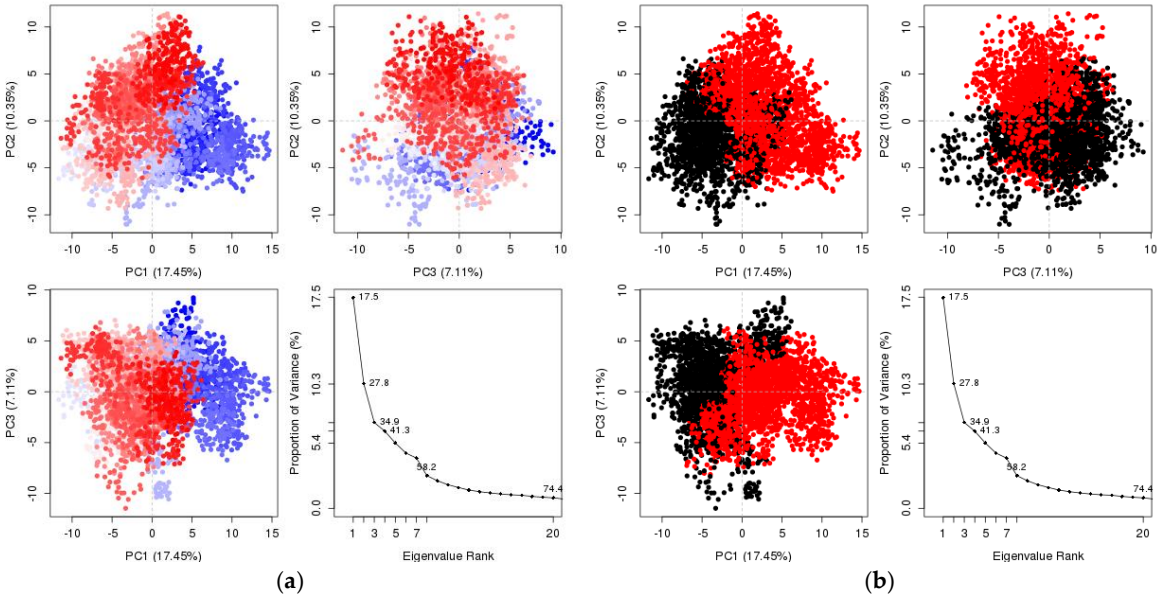

Figure S6. (**a**) Principal Component Analysis (PCA) concerning the MD trajectory of the binding of CID #526 to the RBD of wild-type SARS-CoV-2. The trajectory frames are colored from blue to white to red, which corresponds to their order with respect to time. (**b**) Simple clustering in PC subspace. The conformations were divided into two clusters (black and red) according to the top three PC spaces shown in the PC subspace.

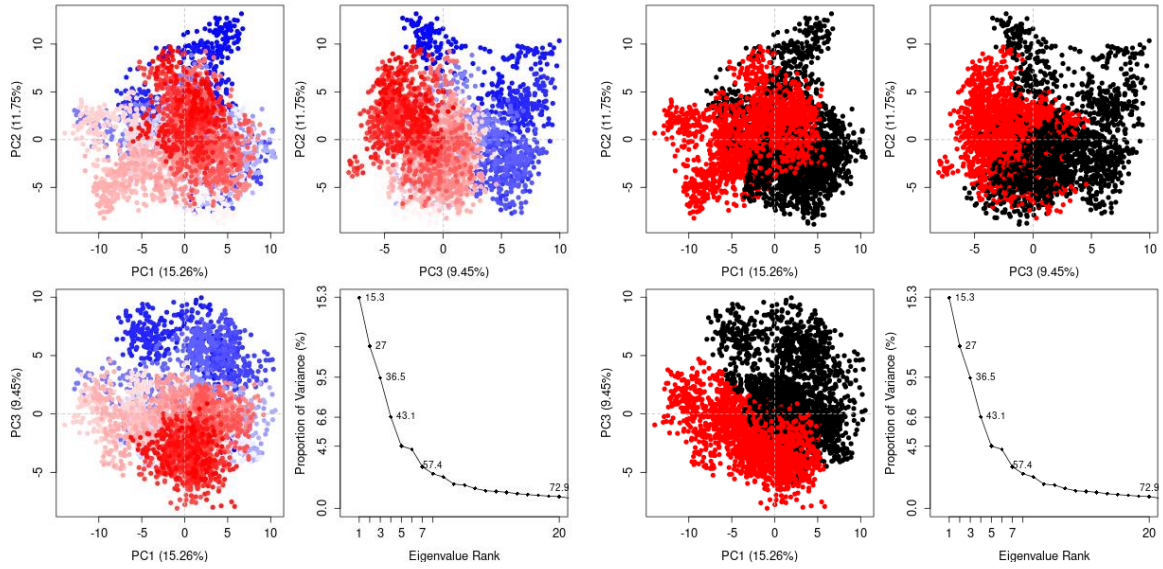

(**a**) (**b**)

Figure S7. (**a**) Principal Component Analysis (PCA) concerning the MD trajectory of the unbinding of CID #526 to the RBD of wild-type SARS–CoV–2. The trajectory frames are colored from blue to white to red, which corresponds to their order with respect to time. (**b**) Simple clustering in PC subspace. The conformations were divided into two clusters (black and red) according to the top three PC spaces shown in the PC subspace.

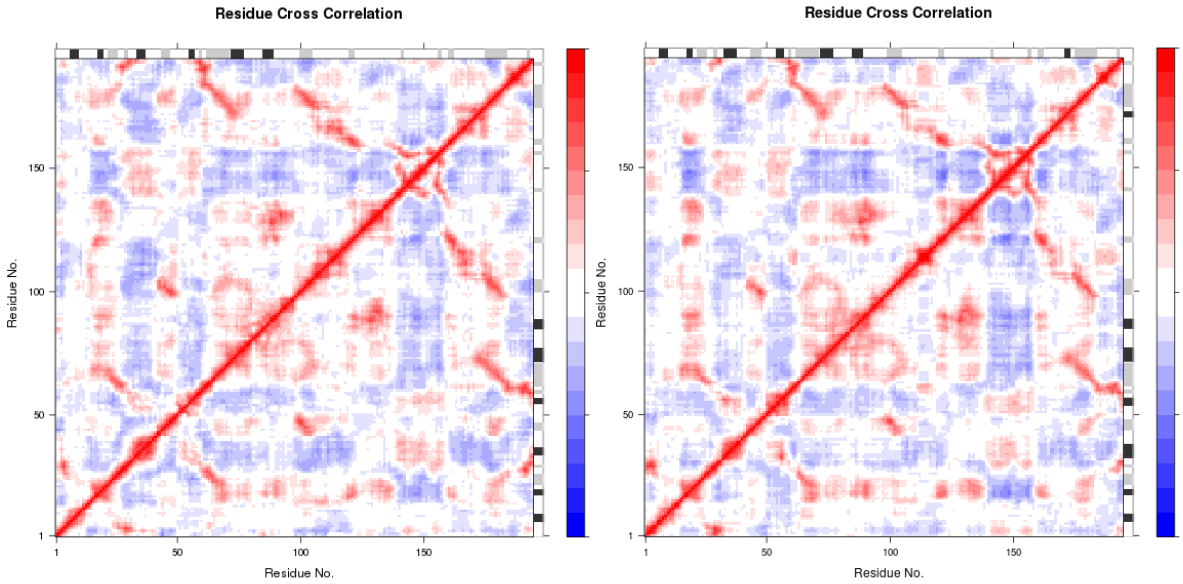

(**a**) (**b**)

Figure S8. Dynamical residue cross-correlation map for the MD trajectory of the (**a**) binding process and (**b**) unbinding process of the receptor–ligand complex involving CID #526 docked in the RBD of wild-type SARS-CoV-2. PCA results regarding trajectory with trajectory frames colored from blue to white to red, which corresponds to their order with respect to time.

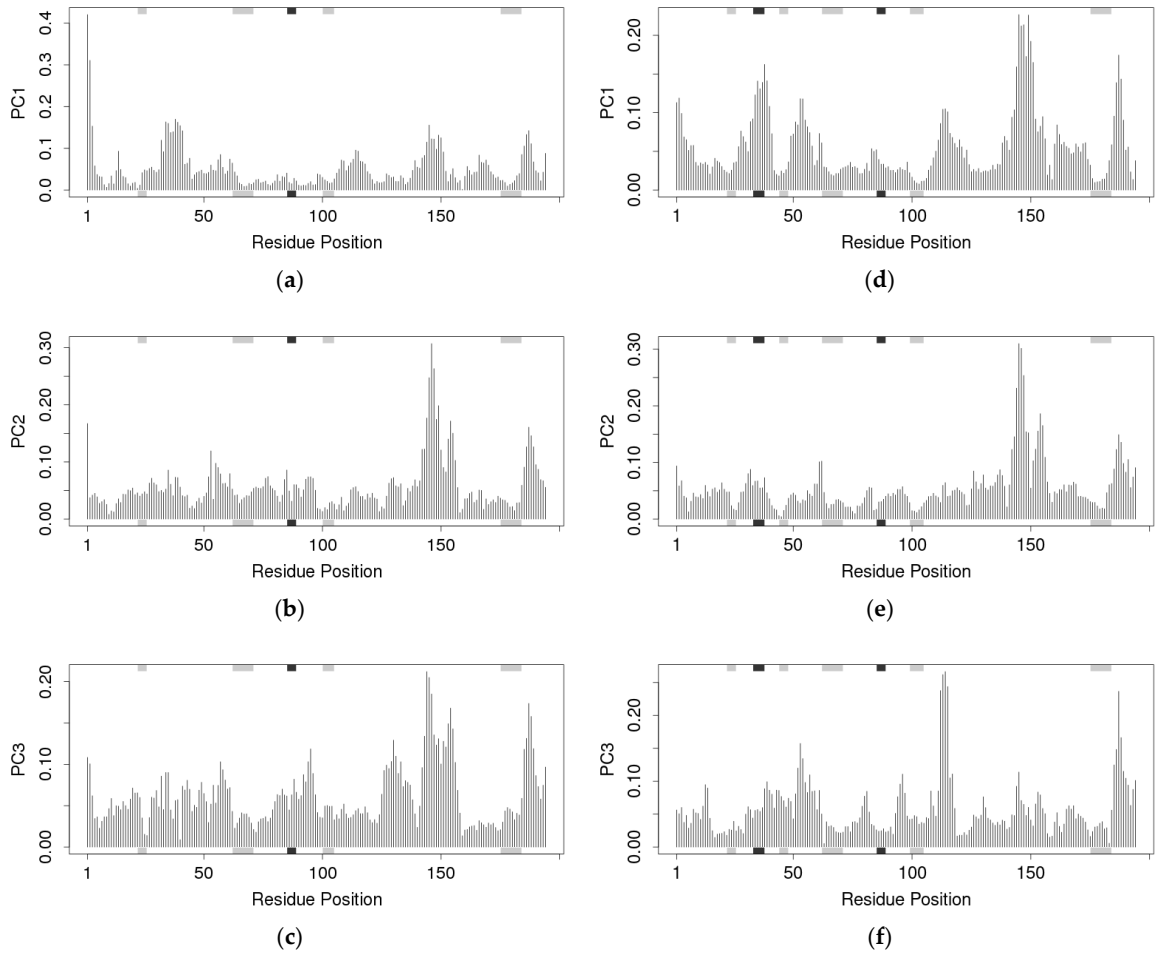

Figure S9. Residue-wise loading for (**a**) PC1, (**b**) PC2, and (**c**) PC3 of the binding process of the receptor–ligand complex involving CID #526 docked in the RBD of wild-type SARS-CoV-2. Residue-wise loading for (**d**) PC1, (**e**) PC2, and (**f**) PC3 of the unbinding process of the receptor–ligand complex involving CID #526 docked in wild-type SARS-CoV-2.

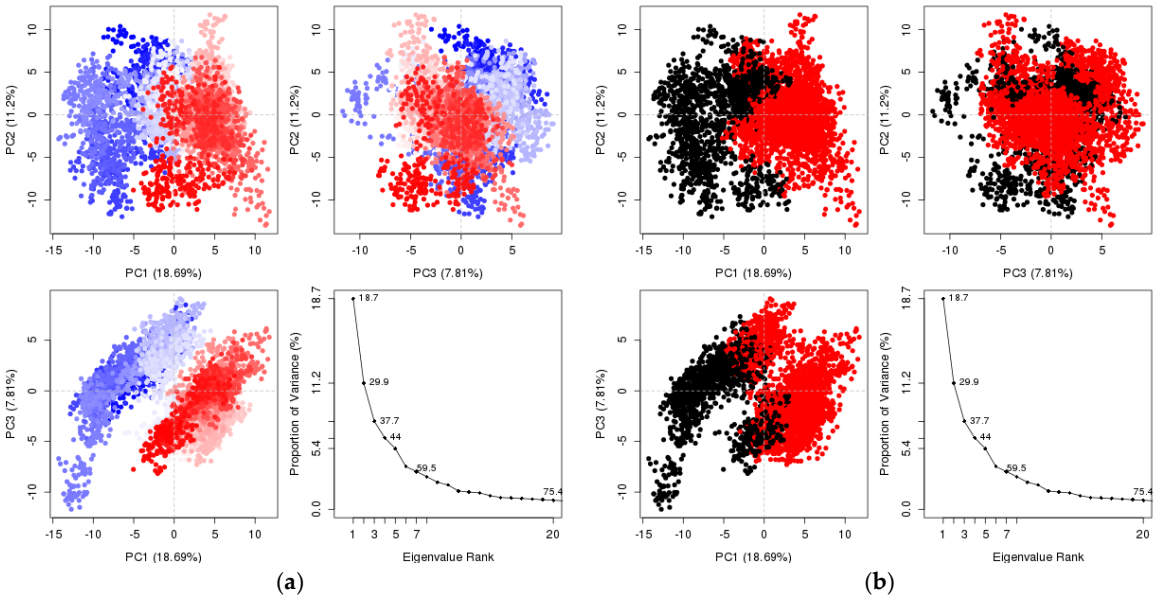

Figure S10. (**a**) Principal Component Analysis (PCA) concerning the MD trajectory of the binding of CID #526 to the RBD of the B.1.1.7 variant of SARS-CoV-2. The trajectory frames are colored from blue to white to red, which corresponds to their order with respect to time. (**b**) Simple clustering in PC

subspace. The conformations were divided into two clusters (black and red) according to the top three PC spaces shown in the PC subspace.

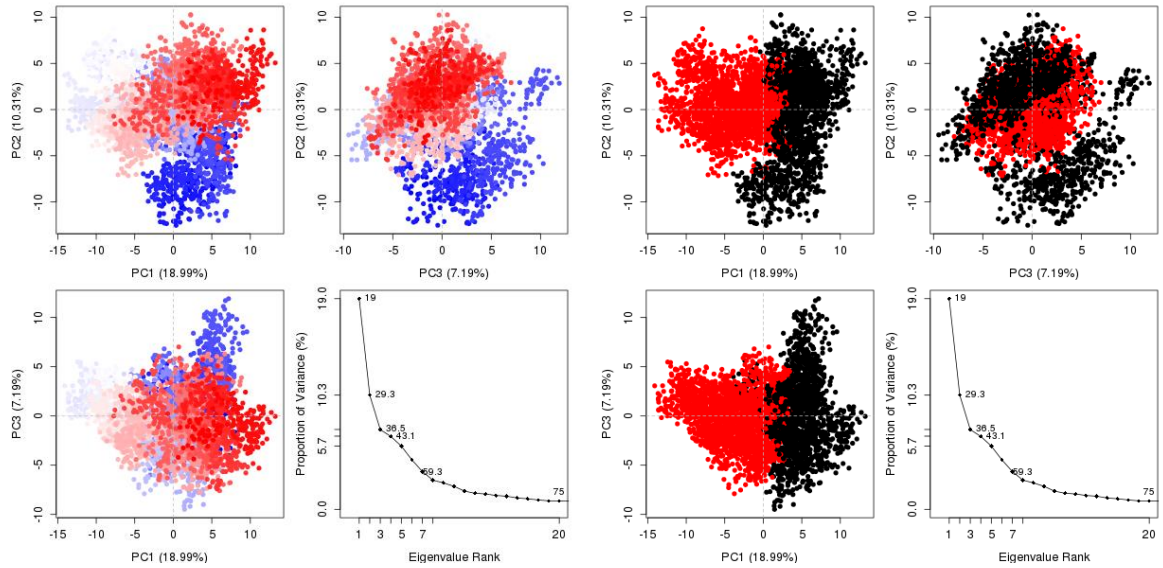

Figure S11. (**a**) Principal Component Analysis (PCA) concerning the MD trajectory of the binding of CID #526 to the RBD of the B.1.1.7 variant of SARS-CoV-2. The trajectory frames are colored from blue to white to red, which corresponds to their order with respect to time. (**b**) Simple clustering in PC subspace. The conformations were divided into two clusters (black and red) according to the top three PC spaces shown in the PC subspace.

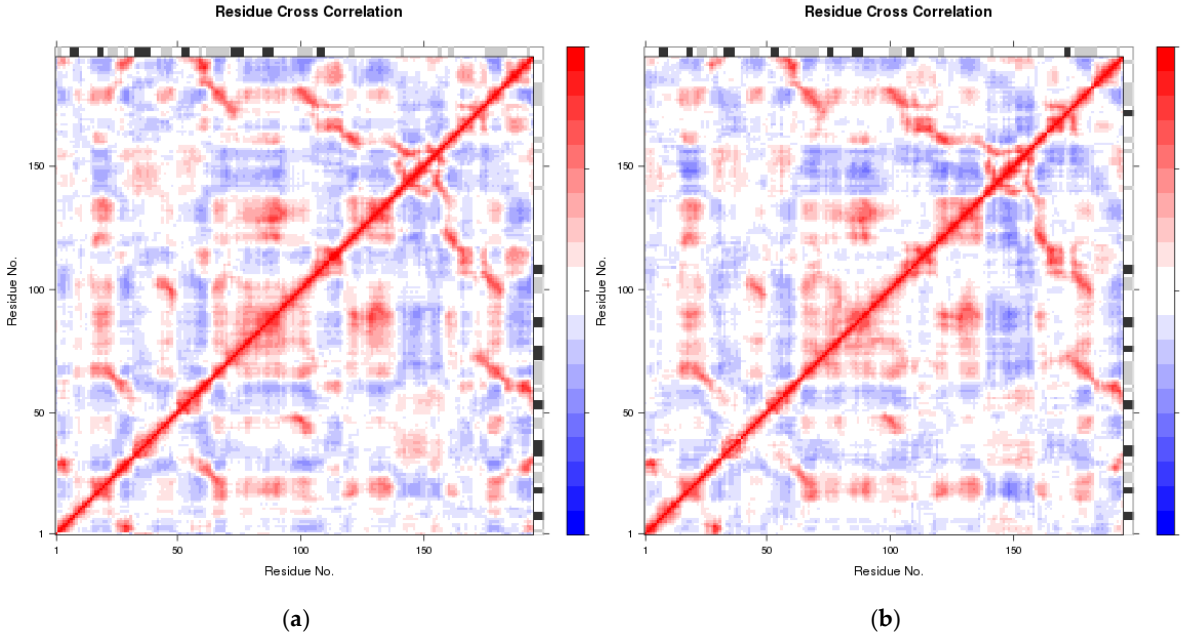

Figure S12. Dynamical residue cross-correlation map for the MD trajectory of the (**a**) binding process and (**b**) unbinding process of the receptor–ligand complex involving CID #526 docked in the RBD of the B.1.1.7 variant of SARS-CoV-2. PCA results for trajectory with trajectory frames colored from blue to white to red, which corresponds to their order with respect to time.

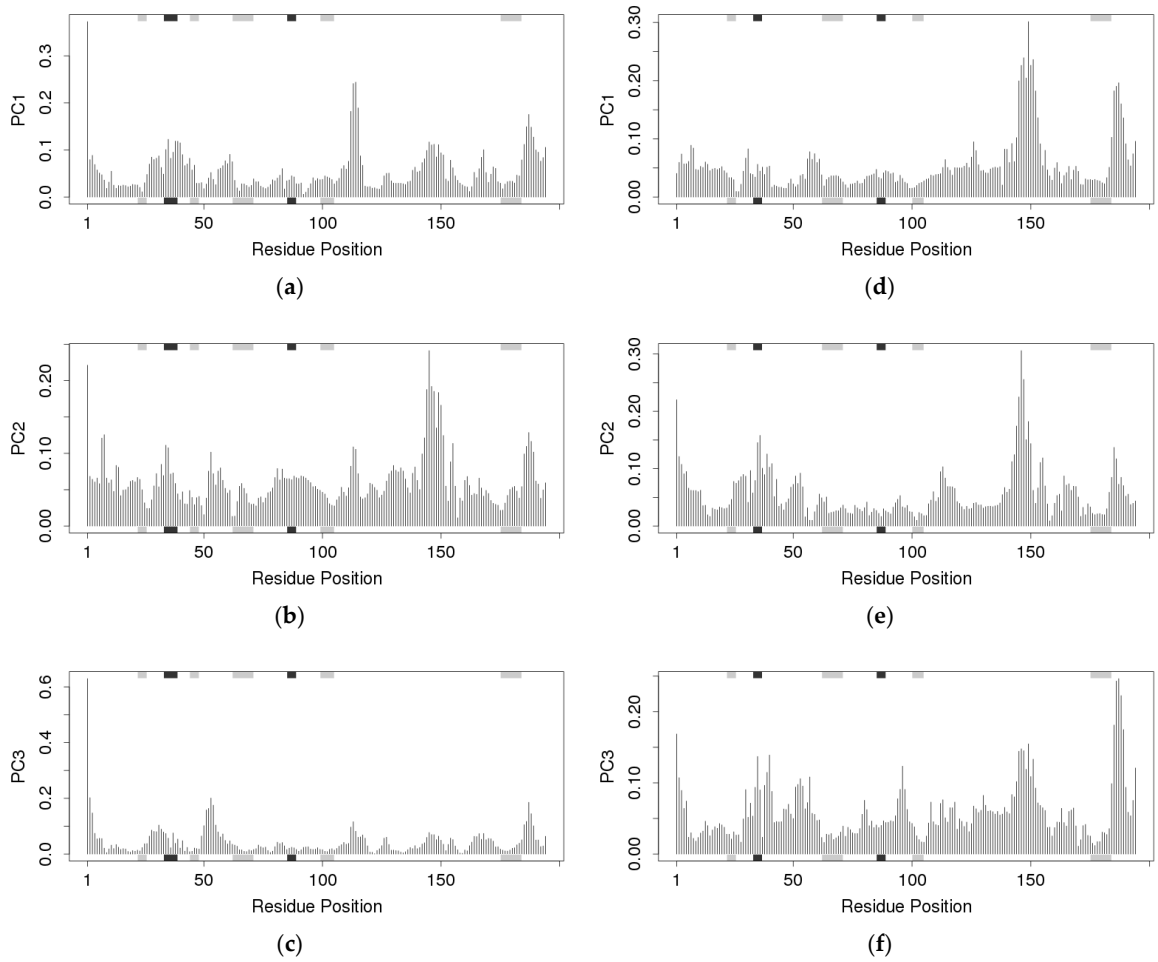

Figure S13. Residue-wise loading for (**a**) PC1, (**b**) PC2, and (**c**) PC3 of the binding process of the receptor–ligand complex involving CID #526 docked in the RBD of the B.1.1.7 variant of SARS-CoV-2. Residue-wise loading for (**d**) PC1, (**e**) PC2, and (**f**) PC3 of the unbinding process of the receptor–ligand complex involving CID #526 docked in the B.1.1.7 variant of SARS-CoV-2.

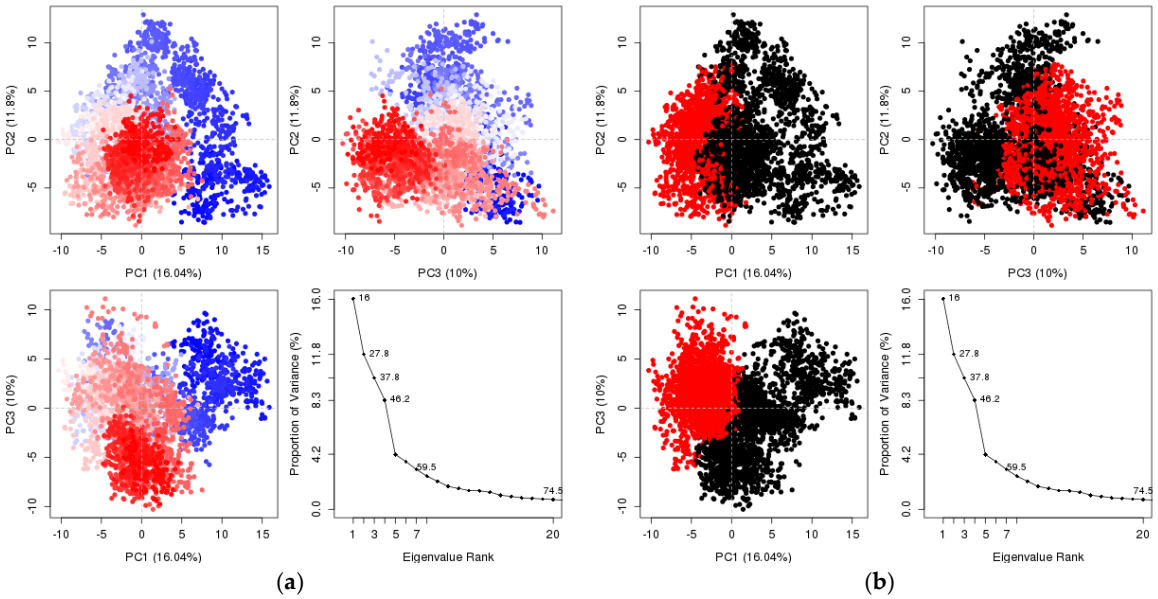

Figure S14. (**a**) Principal Component Analysis (PCA) concerning the MD trajectory of the binding of CID #526 to the RBD of the B.1.351 variant of SARS–CoV–2. The trajectory frames are colored from blue to white to red, which corresponds to their order with respect to time. (**b**) Simple clustering in

PC subspace. The conformations were divided into two clusters (black and red) according to the top three PC spaces shown in the PC subspace.

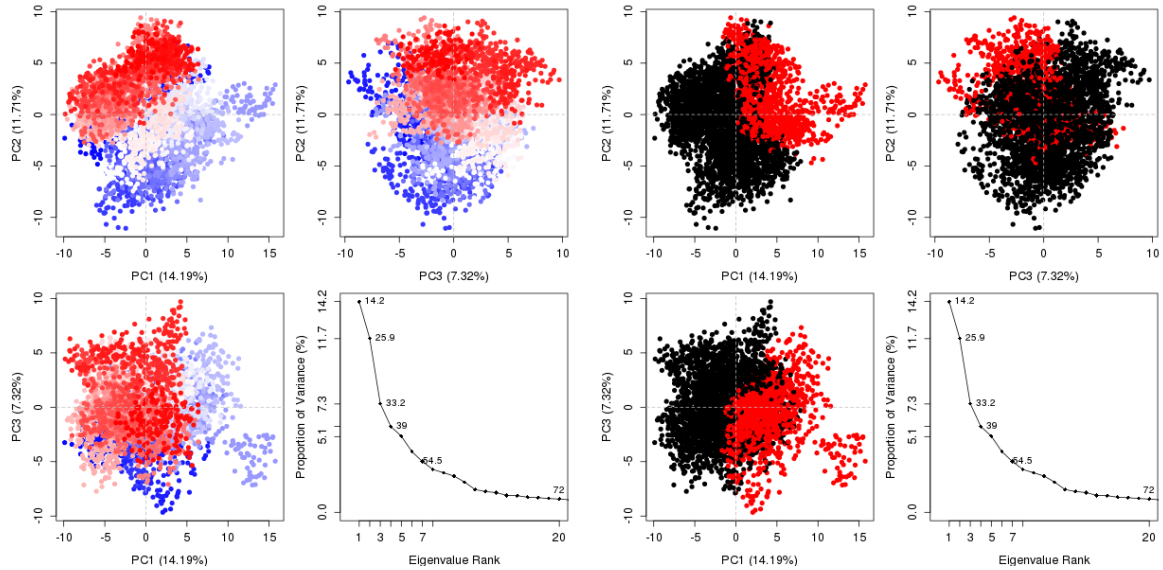

Figure S15. (**a**) Principal Component Analysis (PCA) concerning the MD trajectory of the binding of CID #526 to the RBD of the B.1.351 variant of SARS−CoV−2. The trajectory frames are colored from blue to white to red, which corresponds to their order with respect to time. (**b**) Simple clustering in PC subspace. The conformations were divided into two clusters (black and red) according to the top three PC spaces shown in the PC subspace.

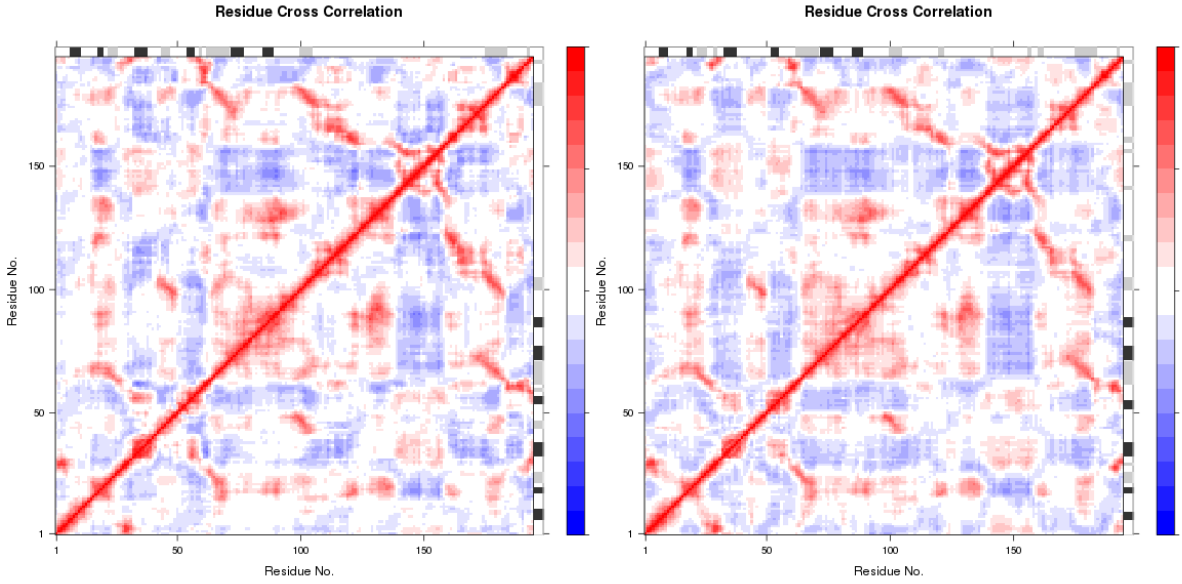

Figure S16. Dynamical residue cross-correlation map for the MD trajectory of the (**a**) binding process and (**b**) unbinding process of the receptor–ligand complex involving CID #526 docked in the RBD of the B.1.351 variant of SARS-CoV-2. PCA results for trajectory with trajectory frames colored from blue to white to red, which corresponds to their order with respect to time.

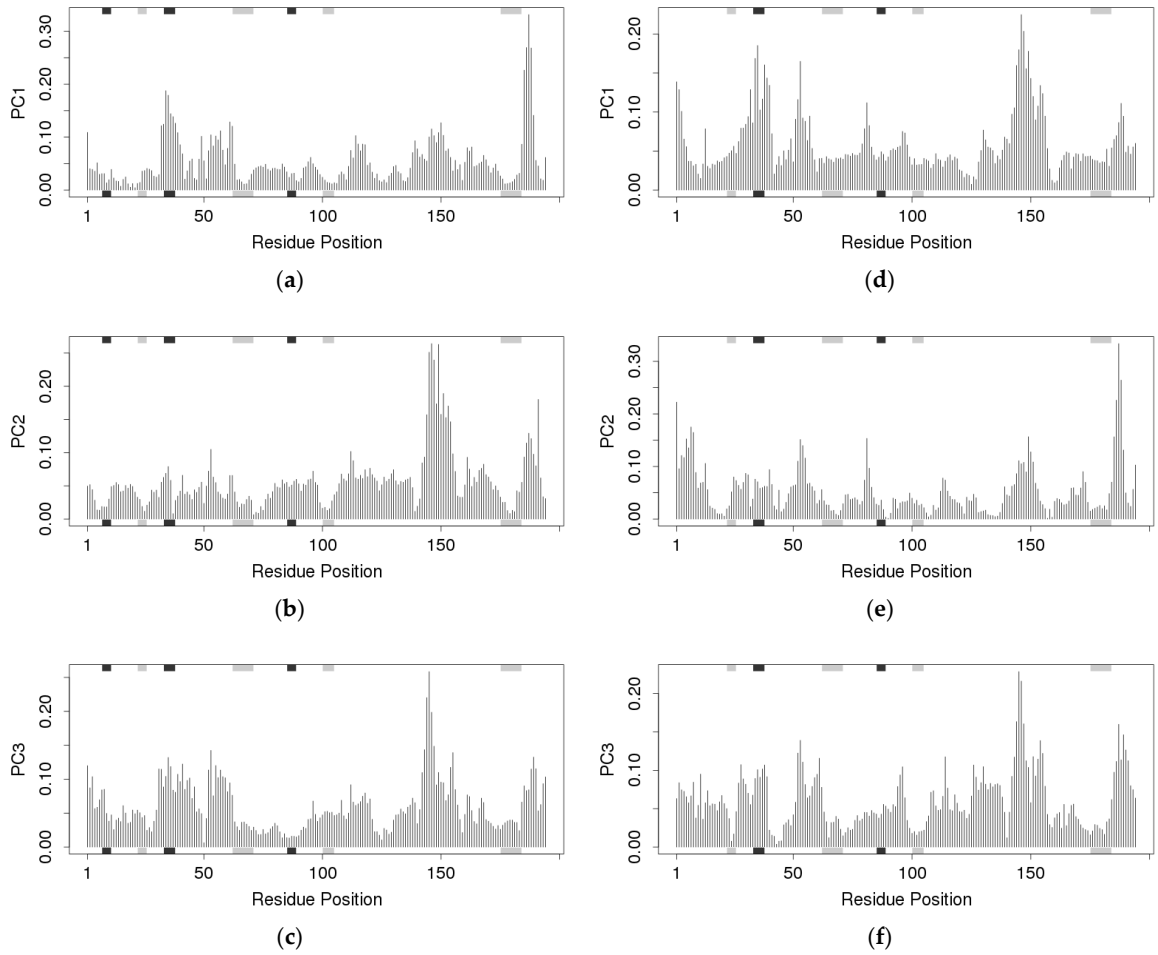

Figure S17. Residue-wise loading for (**a**) PC1, (**b**) PC2, and (**c**) PC3 of the binding process of the receptor–ligand complex involving CID #526 docked in the RBD of the B.1.351 variant of SARS-CoV-2. Residue-wise loading for (**d**) PC1, (**e**) PC2, and (**f**) PC3 of the unbinding process of the receptor–ligand complex involving CID #526 docked in the B.1.351 variant of SARS-CoV-2.

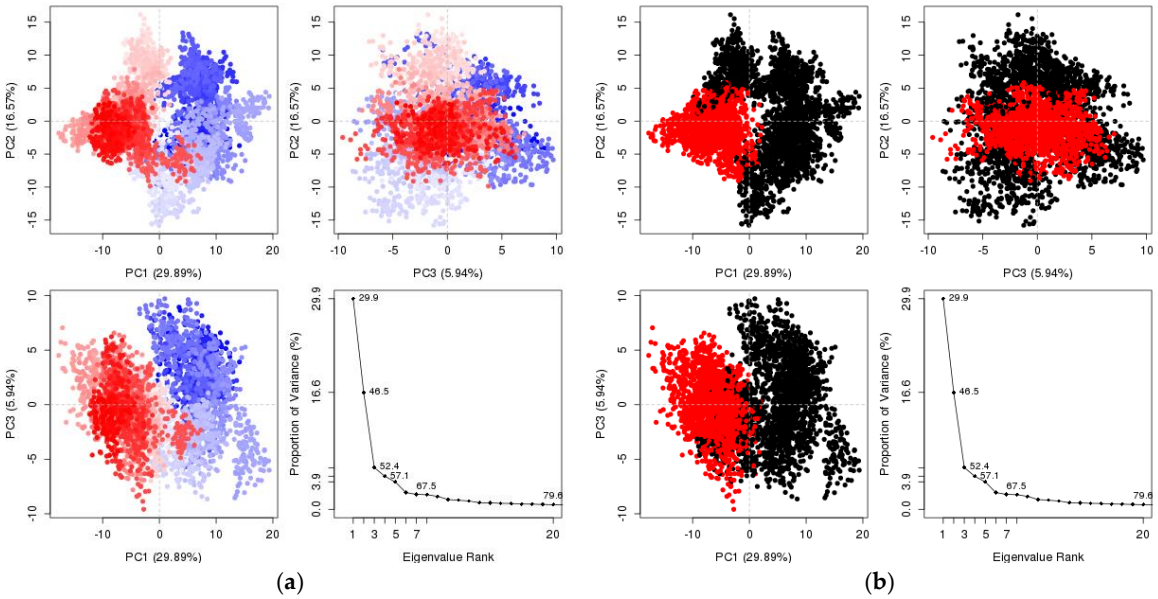

Figure S18. (**a**) Principal Component Analysis (PCA) concerning the MD trajectory of the binding of CID #526 to the RBD of P.1 variant of SARS-CoV-2. The trajectory frames are colored from blue to white to red, which corresponds to their order with respect to time. (**b**) Simple clustering in PC

subspace. The conformations were divided into two clusters (black and red) according to the top three PC spaces shown in the PC subspace.

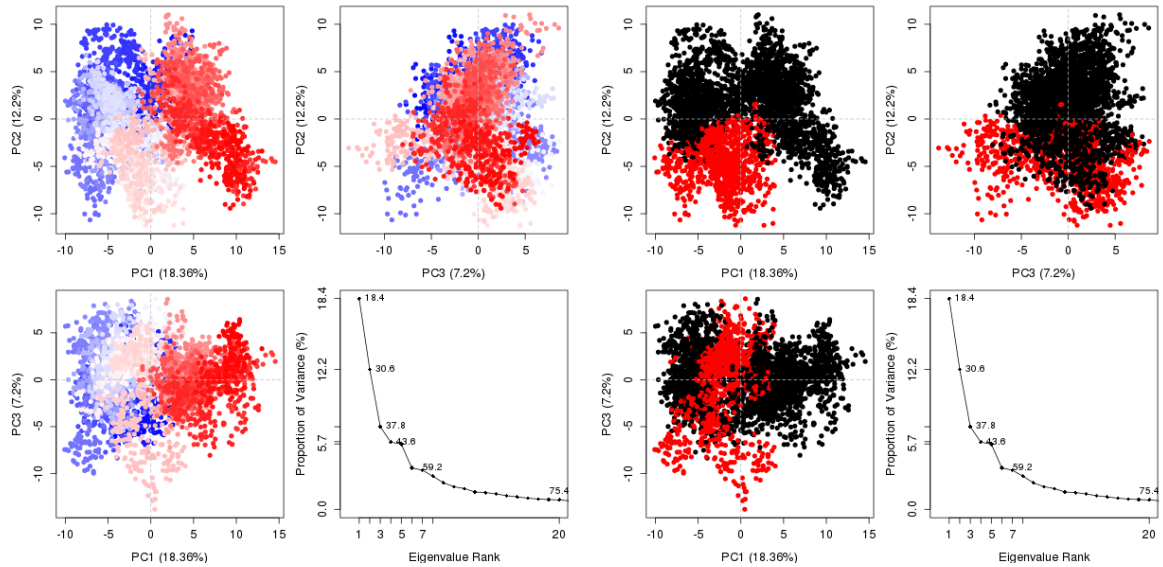

Figure S19. (**a**) Principal Component Analysis (PCA) concerning the MD trajectory of the binding of CID #526 to the RBD of P.1 variant of SARS-CoV-2. The trajectory frames are colored from blue to white to red, which corresponds to their order with respect to time. (**b**) Simple clustering in PC subspace. The conformations were divided into two clusters (black and red) according to the top three PC spaces shown in the PC subspace.

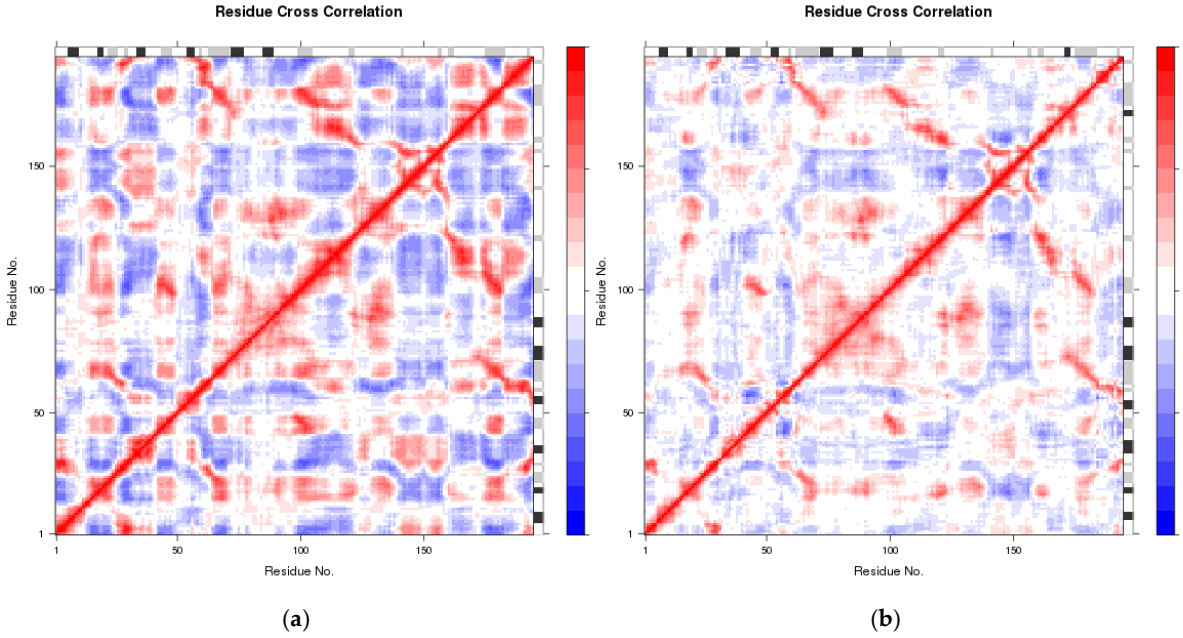

Figure S20. Dynamical residue cross-correlation map for the MD trajectory of the (**a**) binding process and (**b**) unbinding process of the receptor–ligand complex involving CID #526 docked in the RBD of P.1 variant SARS CoV-2. PCA results for trajectory with trajectory frames colored from blue to white to red, which corresponds to their order with respect to time.

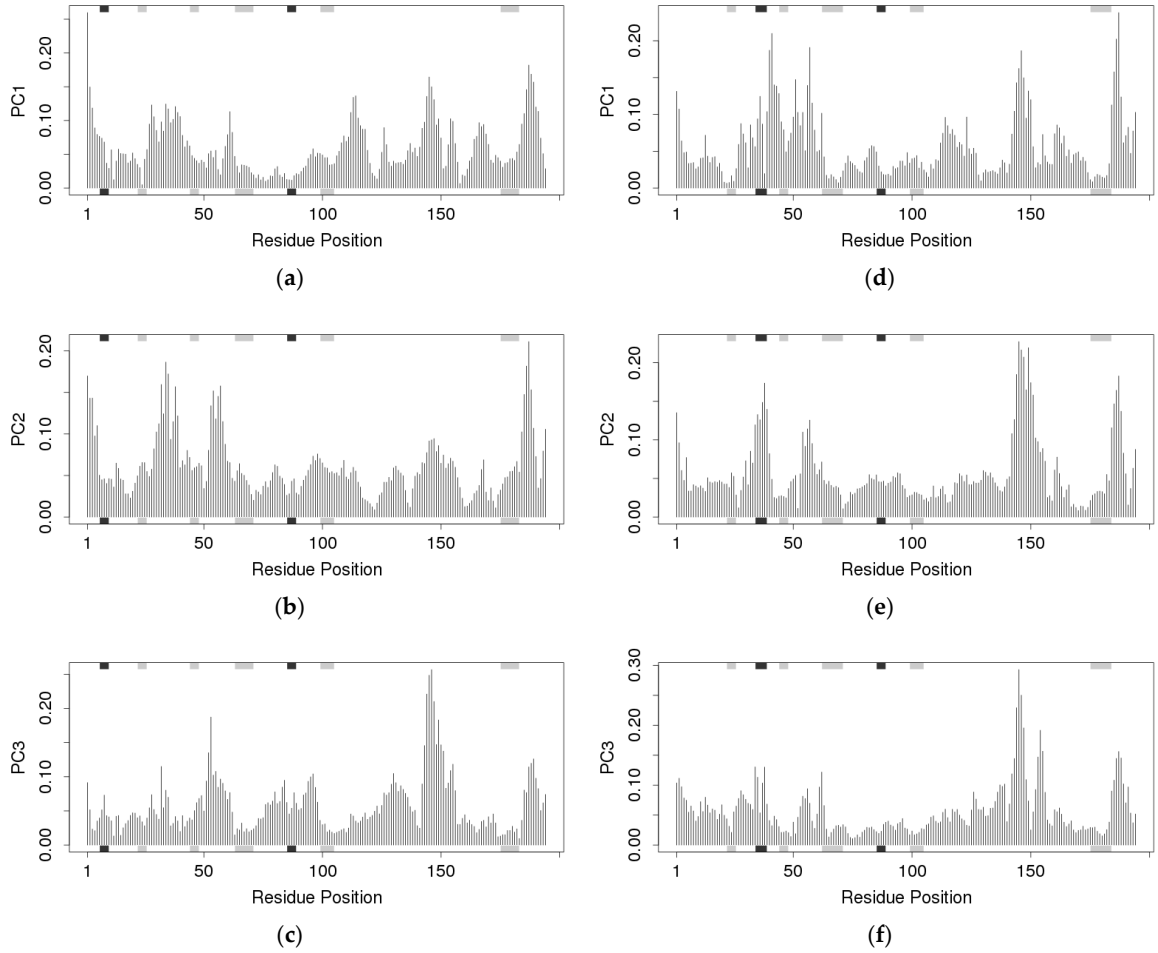

Figure S21. Residue-wise loading for (**a**) PC1, (**b**) PC2, and (**c**) PC3 of the binding process of the receptor–ligand complex involving CID #526 docked in the RBD of P.1 variant of SARS-CoV-2. Residue-wise loading for (**d**) PC1, (**e**) PC2, and (**f**) PC3 of the unbinding process of the receptor–ligand complex involving CID #526 docked in P.1 variant of SARS-CoV-2.

Table S6. Binding Energy of CID #526 against various variants of SARS-CoV-2.

SARS-CoV-2 Variant	ΔG_{PB} (kcal mol^{-1})
Wild	−6.15
B.1.1.7	−3.85
B.1.351	−6.12
P.1	−5.19